coatings

MDPI

Article

Low-Threshold Optical Bistability Based on Photonic Crystal Fabry–Perot Cavity with Three-Dimensional Dirac Semimetal

Fengyu Li [1], Jiao Xu [2], Jianbo Li [1], Yuxiang Peng [1,*] and Mengdong He [1,*]

[1] Institute of Mathematics and Physics, Central South University of Forestry and Technology, Changsha 410004, China; 18207373677@163.com (F.L.); jbli_opt@csuft.edu.cn (J.L.)
[2] School of Physics and Electronics, Hunan Normal University, Changsha 410081, China; xujiao@hunnu.edu.cn
* Correspondence: yxpeng_opt@126.com (Y.P.); mengdonghe@csuft.edu.cn (M.H.)

Abstract: In this paper, we investigate theoretically the tunable low threshold optical bistability (OB) in the terahertz range based on photonic crystals' Fabry–Perot (FP) cavity with a three-dimensional Dirac semimetal (3D DSM). On the one hand, a 3D DSM with a high nonlinear refractive index coefficient creates conditions for the generation of OB. Additionally, the finite film thickness of 3D DSMs leads to significantly a enhanced interaction volume compared to graphene, which allows easier preparation and has stable properties. On the other hand, the resonance of the FP cavity plays a positive role in promoting the tunable low-threshold OB. It was found that the OB threshold and hysteresis curve can be continuously adjusted by manipulating the Fermi energy and relaxation times of a 3D DSM. Additionally, the bistable curve of the composite structure is also closely related to the angle of incident light. Through parameter optimization, OB with a threshold approaching 10^5 V/m can be obtained. The photonic crystal's FP cavity with a 3D DSM structure provides a feasible way to achieve low-threshold OB and a building block for future integrated all-optical devices.

Keywords: optical bistability; three-dimensional dirac semimetal; photonic crystal; Fabry–Perot cavity

check for updates

Citation: Li, F.; Xu, J.; Li, J.; Peng, Y.; He, M. Low-Threshold Optical Bistability Based on Photonic Crystal Fabry–Perot Cavity with Three-Dimensional Dirac Semimetal. *Coatings* **2023**, *13*, 936. https://doi.org/10.3390/coatings13050936

Academic Editor: Piotr Potera

Received: 21 April 2023
Revised: 12 May 2023
Accepted: 14 May 2023
Published: 17 May 2023

Copyright: © 2023 by the authors. Licensee MDPI, Basel, Switzerland. This article is an open access article distributed under the terms and conditions of the Creative Commons Attribution (CC BY) license (https://creativecommons.org/licenses/by/4.0/).

1. Introduction

The development of optical nonlinear devices controlled by light is a long-standing goal in the field of all-optical communication research. Optical bistability (OB), as a typical optical nonlinear phenomenon, has caused widespread concern because of its potential applications in optical devices such as all-optical switches [1], optical transistors [2], optical modulators [3], optical storage [4], optical logic gates [5], and so on. However, conventional optical-bistablility devices have large dimensions and require stronger incident light conditions to achieve significant OB phenomena, thus creating an obstacle to the practical implementation of OB devices. In recent years, with the development of micro-nano technology, researchers have started to pay attention to OB phenomena in micro-nano structures, such as photonic crystals [6], dielectric gratings [7], metamaterials [8], optical cavity ring resonators [9], etc. High-frequency electromagnetic fields can be continuously oscillated within the resonant cavity, and the interaction between the optical field and the material can be enhanced. These further enhance the optical nonlinear effects in the cavity at low input intensities. Therefore, the preparation of micro-resonant cavities is of great importance for optical integrated devices. Photonic crystals (PhCs) have a unique ability to manipulate light in terms of reflection, localization, and modulation, making them one of the important materials for micro and nano optoelectronic integration [10]. Compared with silver mirrors, photonic crystals have the characteristics of ultra-compact size, excellent resonance performance, flexible structure design and so on [11]. Thus, PhCs with unique bandgap structures can be used to design and fabricate small and easily tunable resonant cavities [12]. The idea of using photonic crystal structures instead of mirrors in a Fabry–Perot (FP) cavity to fabricate optical devices with resonant modes and tunable

characteristics is seeing acceptance. Optical devices based on the PhC FP cavity such as optical absorption devices [13], optical filters [14], slow-light and nonlinear devices [15], multiplexers [16], and optical 1-bit comparator [17,18] have also been reported.

It is well-known that OB can be achieved by filling the FP cavity with a nonlinear medium [19]. The reduction in the threshold value of OB is limited since the nonlinear coefficients of most materials are relatively low. In recent years, low-threshold tunable OB based on graphene has been widely studied due to the excellent nonlinear properties of the two-dimensional material graphene. Although the two-dimensional Dirac material graphene also exhibits extremely high nonlinearity in theory [20–22] and experiments [23–25], its atomically thin feature leads to relatively small interaction volumes and it has low stability, thus limiting the research of graphene in nonlinear fields such as all-optical switching [26]. A new topological material with linear energy dispersion, the three-dimensional Dirac semimetal (3D DSM) has started to receive attention [27–31]. 3D DSMs are often regarded as '3D graphene' in which exotic quantum phenomena such as chiral magnetic effects [32,33], high bulk carrier mobility [34] and large nonsaturating magnetoresistance [35] are commonly observed. At present, many materials have been confirmed to be three-dimensional Dirac semimetals, such as Cd_3As_2 [36], $PtTe_2$ [37], Na_3Bi [38], $ZrTe_5$ [39], etc. The finite film thickness of 3D DSM leads to a significantly enhanced interaction volume compared to graphene, and 3D DSM possesses higher carrier mobility [40], a higher Fermi velocity [41], the ability for easier preparation and stable properties [42]. In particular, the Dirac band structure of 3D DSMs has a high nonlinear refractive index coefficient, which is very similar to that of graphene. At the same time, 3D DSMs can modulate the dielectric constant v changing the Fermi energy level [43]. The high nonlinear refractive index of 3D Dirac semimetals is expected to play an important role in providing strong optical nonlinearity for achieving low-threshold OB.

In this paper, graphene is replaced by the more advantageous 3D DSM, and a simple structure of 3D DSM embedded in the PhC FP cavity is proposed. It is shown that local electric field enhancement is generated in the PhC FP cavity. In addition, the introduction of 3D DSM into the overall structure can provide good conditions for a reduction in the OB threshold. Meanwhile, the threshold of OB can be dynamically adjusted by changing the Fermi energy level and relaxation time of the Dirac material. This low-threshold OB scheme has the characteristics of a simple structure and easy preparation, and we believe that it is expected to provide new ideas for the development of all-optical communication devices.

2. Theoretical Model and Method

We consider a FP cavity with two symmetric photonic crystals and place the 3D DSM in the middle of the cavity, as shown in Figure 1. Additionally, we set the direction perpendicular to the photonic crystal to be the z-direction. The photonic crystal consists of alternating dielectrics, A and B, with a period of 4. The thicknesses of media A and B are set to $d_a = \Lambda_c/(4\mathrm{n}_a)$, $\mathrm{d}_b = \Lambda_c/(4\mathrm{n}_b)$, where Λ_c is the central wavelength, and Λ_c= 300 μm is set here. The thickness of the Dirac semi-metallic layer is set to $d_{Dirac} = 20$ nm. We take polymethylpentene (TPX) with a refractive index of $\mathrm{n_a}$ = 1.46 for medium A and SiO_2 with a refractive index of $\mathrm{n_b}$ = 1.9 for medium B. The cavity length of the FP cavity is denoted as L, and middle of the cavity is filled with empty air. We place the 3D DSM in the middle of the cavity and set $L = 2L_l = 2L_r = 300$ μm. Based on the current mature technology for the preparation of micro/nano multilayer dielectric structures, it is possible to construct the layered structure defined by the above structural parameters. Meanwhile, 3D DSM can be characterized by third-order nonlinear susceptibility and linear refractive index as a typical Kerr nonlinear medium. To obtain large nonlinear coefficients, we consider only the incident waves in the terahertz band.

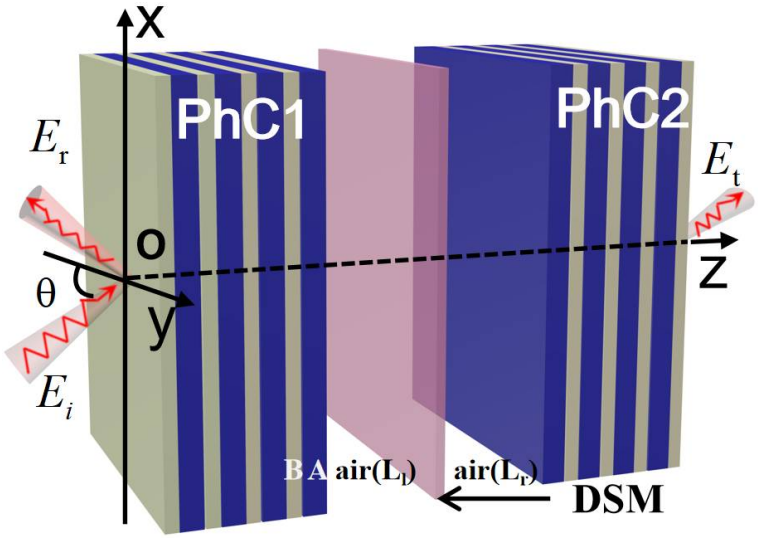


Figure 1. Schematic structure based on 3D DSM/PhC FP cavity's heterostructure.

Based on the classical Boltzmann transport equation under the relaxation time approximation, the 3D DSM linear in-band optical conductivity can be resolved as follows [44]:

$$\sigma_1 = \sigma_0 \frac{4}{3\pi^2} \frac{\tau}{1 - i\omega\tau} \frac{(k_B T)^2}{\hbar^2 v_F} \left[2Li_2\left(-e^{-\frac{E_F}{k_B T}}\right) + \left(\frac{E_F}{k_B T}\right)^2 + \frac{\pi^2}{3} \right], \tag{1}$$

where $\sigma_0 \equiv \frac{e^2}{4\hbar}$, ω is the angular frequency, k_B is the Boltzmann constant, $\hbar$ is the Planck constant, T is the temperature, v_F is the Fermi velocity of the electron, and τ and E_F represent the relaxation time and Fermi energy level of the 3D DSM, respectively. $Li_s(z)$ is the multilogarithmic function. Considering an external field, the third-order nonlinear optical conductivity of the 3D DSM can be expressed as follows [44]:

$$\sigma_3 = \sigma_0 \frac{8e^2 v_F}{5\pi^2 \hbar^2} \frac{\tau^3}{(1 + \omega^2\tau^2)(1 - 2i\omega\tau)} \frac{1}{1 + \exp\left(-\frac{E_F}{k_B T}\right)}. \tag{2}$$

Thus, we can obtain the third-order nonlinear susceptibility, $\chi^{(3)}$, and linear refractive index, n_D, of the 3D DSM:

$$\begin{cases} \chi^{(3)} = i\sigma_3/\varepsilon_0\omega \\ n_D = n + ik = \sqrt{1 + i\sigma_1/\varepsilon_0\omega} \end{cases}, \tag{3}$$

where ε_0 is the dielectric constant in vacuum. From Equation (3), it can be seen that the third-order nonlinear polarizability, $\chi^{(3)}$, and linear refractive index, n_D, of the 3D DSM are strongly affected by its Fermi energy and relaxation time, which provides us with an effective method with which to modulate OB devices based on Dirac semimetals.

In accordance with the nonlinear transport matrix method, we have obtained the transport matrix corresponding to each layer of the medium. Hence, the transmission matrix of the overall structure is

$$M = (M_B \times M_A)^4 \times M_{air} \times M_D \times M_{air} \times (M_A \times M_B)^4. \tag{4}$$

Therefore, the transmission and reflection coefficients can be expressed as follows:

$$\begin{cases} t = \frac{2p_f}{[M_{11} + M_{12}p_f]p_f + [M_{21} + M_{22}p_f]} \\ r = \frac{[M_{11} + M_{12}p_f]p_f - [M_{21} + M_{22}p_f]}{[M_{11} + M_{12}p_f]p_f + [M_{21} + M_{22}p_f]} \end{cases}. \tag{5}$$

where $p_f = \left(k_0^2 - k_y^2\right)^{\frac{1}{2}}/k_0$. Finally, we can obtain the relationship between the incident electric field, E_{in}, and the transmitted electric field, E_{out}, as well as the reflected electric field, E_{re}:

$$\begin{cases} |E_{out}| = |E_{in}| \times |t|^2 \\ |E_{re}| = |E_{in}| \times |r|^2 \end{cases}, \quad (6)$$

where the OB phenomenon can be observed by adjusting the relevant parameters.

3. Results and Discussions

First, the electric field distribution of the heterogeneous structure of a photonic crystal's FP cavity is calculated, as shown in Figure 2. It can be seen that distinct electric field localization appears at the 3D DSM, which provides the conditions for achieving a low-threshold OB. It is well-known that the third-order nonlinear conductivity of Dirac materials is related to the frequency of the incident light, and the higher the frequency of the incident light, the lower its third-order nonlinear conductivity. In this paper, we have investigated the effect of 3D DSM parameters on OB based on the 1 THz frequency range, when the third-order nonlinear conductivity of Dirac material is strong. Meanwhile, the 3D DSM, as a typical Kerr medium, has a complex refractive index including both linear and nonlinear components, and its relationship with the electric field can be expressed as $n = n_D + \Delta n = n_D + n_2|E|^2$, where $n_2 = \frac{\chi^{(3)}}{2n_D}$ is the nonlinear refraction coefficient. Moreover, the local electric field enhancement caused by the FP cavity structure has a positive effect on the nonlinear part of the 3D DSM refractive index. In summary, we can embed a 3D DSM in a 1D PhC FP cavity structure to achieve low-threshold tunable OB phenomena.

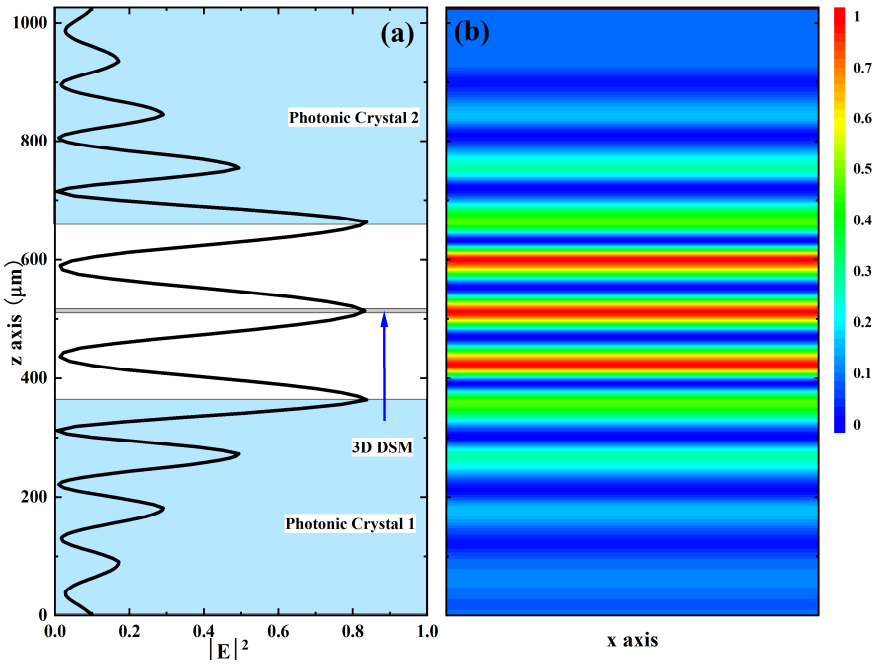


Figure 2. (**a**) The normalized electric field for PhC heterostructures. (**b**) The color map of electric field for PhC heterostructures.

Next, we discuss the role of the relevant parameters of the 3D DSM in the modulation of OB. To facilitate the analysis of the generation mechanism of OB, we assume the thickness of the 3D DSM to be the same as that of a layer of 2D thin film material, similarly to graphene. Then, the bulk conductivity of 3D DSM can be equated to the surface conductivity, that

is $\sigma = d_{DSM}\left(\sigma_1 + \sigma_3|E|^2\right)$. According to reference [45], the expression of the transport matrix of the equivalent 3D DSM is given by

$$M_d = \begin{bmatrix} 1+\Lambda & \Lambda \\ -\Lambda & 1-\Lambda \end{bmatrix}. \tag{7}$$

Meanwhile, we can consider the two PhCs two Bragg mirrors, and their transport matrix can be expressed as follows:

$$M_i \approx \frac{1}{t_i}\begin{bmatrix} -1 & -|r_i| \\ |r_i| & 1 \end{bmatrix}, \tag{8}$$

where $i = \{1, 2\}$, and t_i and r_i are the transmittance and reflectance of the photonic crystal, respectively. The transmission matrix of the air layer can be expressed as follows:

$$M_{air}(L) = \begin{bmatrix} e^{-ikL} & 0 \\ 0 & e^{ikL} \end{bmatrix}. \tag{9}$$

Then, the expression of the transmission matrix of the overall structure is $M = M_{phc1}M_{air}(L_l)M_{DSM}M_{air}(L_r)M_{phc2}$. Based on the definition of the transmission coefficient, we write the relationship between the transmitted electric field, E_t, and the incident electric field, E_i, as follows:

$$\frac{E_t}{E_i} = \frac{1}{M_{11}} = \frac{t_1 t_2}{\Lambda[1 + |r_1||r_2|] + 1 - |r_1||r_2|}, \tag{10}$$

where $\Lambda = d_{DSM}\mu_0 c\left(\sigma_1 + \sigma_3|E_t|^2\right)/2$. Assume that the transmitted electric field is purely real, such that $Y = |E_i|^2$, $X = |E_t|^2$, $k = [1 + |r_1||r_2|]$, and $Z = d_{DSM}\mu_0 c/2$, $p = 1 - |r_1||r_2|$; after calculation and simplification, the above equation can be written as follows:

$$Y = \frac{[Zk(\sigma_1 + \sigma_3 X) + p]^2}{(t_1 t_2)^2} X = \frac{(Zk\sigma_3)^2 X^2 + 2\sigma_1\sigma_3(Zk)^2 X + 2\sigma_3 Zkp X + (Zk\sigma_1)^2 + p^2 + 2Zk\sigma_1 p}{(t_1 t_2)^2} X. \tag{11}$$

From the above equation, it can be seen that Y is a cubic function of X; i.e., the incident electric field is a multivalued function of the transmitted electric field. In order to have three output fields corresponding to one input field, the discriminant, Δ, of the derivative of Equation (15) must be greater than 0. Taking the derivative of Equation (15), the derivative function, Y', can be expressed as follows:

$$Y' = \frac{3(Zk\sigma_3)^2 X^2 + 4\sigma_1\sigma_3(Zk)^2 X + 4\sigma_3 Zkp X + (Zk\sigma_1)^2 + p^2 + 2Zk\sigma_1 p}{(t_1 t_2)^2}. \tag{12}$$

The discriminant, Δ, of the derivative function, Y', can be simplified as folows:

$$\Delta = \frac{\left[2\sigma_3 Zkp + 2\sigma_1\sigma_3(Zk)^2\right]^2}{(t_1 t_2)^4} > 0. \tag{13}$$

From the above equation we can clearly see that Δ always satisfies the condition of being greater than 0, which means that the condition of generating OB is satisfied. Further we can find the extreme and minimal value points of the function Y, i.e., the two zeros of the derivative function:

$$\begin{cases} x_{ext,1} \approx \frac{-\sigma_1}{3\sigma_3} \\ x_{ext,2} \approx \frac{-\sigma_1}{\sigma_3} \end{cases}. \tag{14}$$

The upper and lower thresholds of OB can be found by bringing the maximum and minimum value points into Equation (15), respectively. Further, the width of the hysteresis curve of OB can be expressed as follows:

$$\Delta Y = |Y_1 - Y_2| = \frac{4\sigma_1^3 Z^2 k^2}{27\sigma_3 t_1^2 t_2^2}. \quad (15)$$

$$\Delta Y = \Psi \frac{(1+w^2\tau^2)(1-2iw\tau)}{(1-iw\tau)^3}\left[\left(\frac{E_F}{k_B T}\right)^2 + \frac{\pi^2}{3}\right]^3 \left(1+\exp(-\frac{E_F}{k_B T})\right). \quad (16)$$

where $\Psi = \frac{160(\sigma_0 Zk)^2 (k_B T)^6}{729(\pi\hbar v_F)^4 (et_1 t_2)^2}$. From the above equation, when the Fermi energy level increases, the hysteresis curve width, ΔY, will also increase, which is consistent with the law shown in Figure 3. Meanwhile, from the multivalued function relationship between the transmittance and the incident electric field shown in Figure 3a, it can be seen that the maximum transmittance of the incident wave gradually decreases when the Fermi energy level of the 3D DSM increases from 0.18 eV to 0.24 eV. This indicates that the large Fermi energy of the 3D DSM is lost to some degree upon the transmission of the incident wave. Therefore, the relevant parameters need to be adjusted reasonably when designing low-threshold optically bistable devices to reduce the losses caused by the material. The above results show that the incorporation of the PhC FP cavity with the 3D DSM provide the necessary conditions to realize the OB phenomenon with a low threshold, and the threshold of OB can be controlled by adjusting the Fermi energy level only.

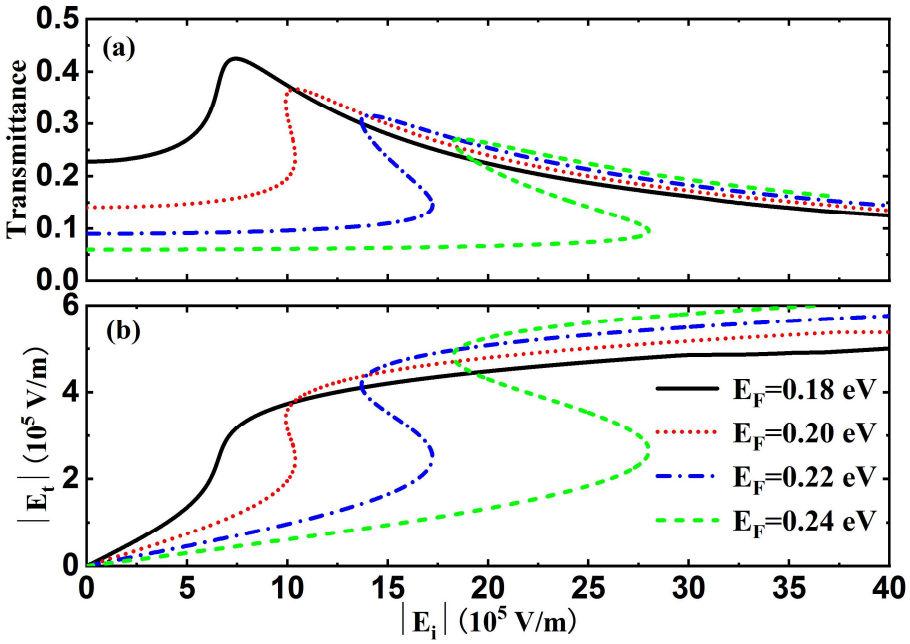


Figure 3. Dependence of (**a**) the transmittance and (**b**) the transmitted electric fields on the incidence electric field for different 3D DSM Fermi energy levels, where $\Lambda = 300$ μm; $\tau = 0.9$ ps, $\theta = 0$ °.

Via the derivation and explanation provided above, the OB phenomenon is closely related to the relaxation time, τ, of the 3D DSM according to Equation (18). As shown in Figure 4, the transmission field and transmittance as a function of the incident field at $E_F = 0.20$ eV is shown. The width and upper/lower thresholds of the OB hysteresis curve vary with the relaxation time, and the variation pattern is consistent with our derived results. As the relaxation time, τ, increases from 0.8 ps to 1.0 ps, the hysteresis curve width of OB increases while the threshold value decreases. Specifically, when the relaxation time is $\tau = 0.8$ ps, the hysteresis curve width is $\Delta Y \approx 0.019 \times 10^6$ V/m, with an upper threshold

of $|E_i|_{up} \approx 1.096 \times 10^6$ V/m, and a lower threshold of $|E_i|_{down} \approx 1.077 \times 10^6$ V/m; when the relaxation time $\tau = 1.0$ ps, the hysteresis curve width $\Delta Y \approx 0.074 \times 10^6$ V/m, upper threshold $|E_i|_{up} \approx 0.996 \times 10^6$ V/m lower threshold $|E_i|_{down} \approx 0.922 \times 10^6$ V/m. Overall, the hysteresis width of OB increases by nearly 0.055×10^6 V/m and the threshold decreases by nearly 0.127×10^6 V/m. It is obvious that the hysteresis width of OB based on 3D DSM changes significantly with the relaxation time, τ.

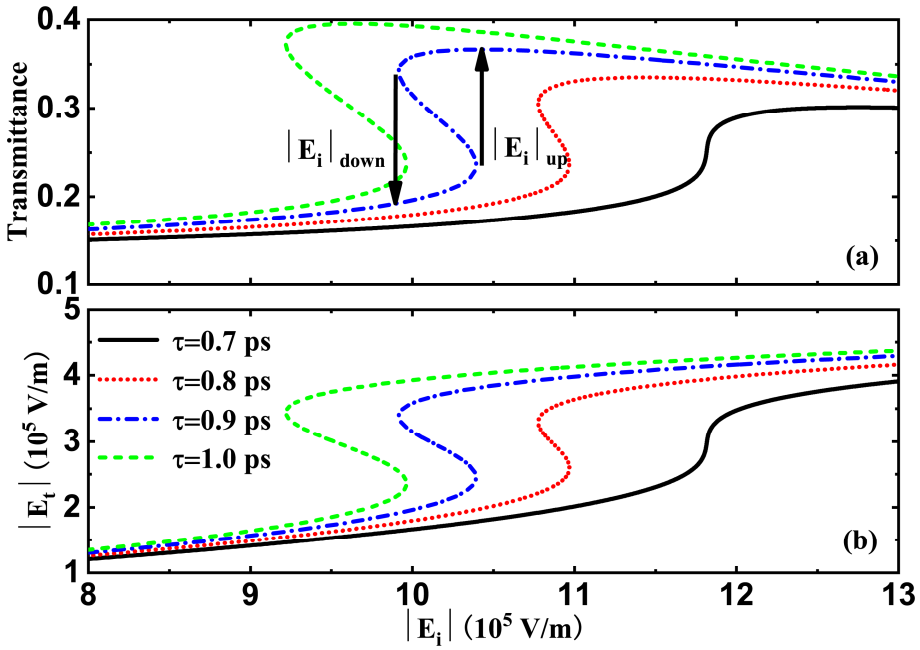


Figure 4. Dependence of (**a**) the transmittance and (**b**) the transmitted electric fields on the incidence electric field for different 3D DSM relaxation times, where $\Lambda = 300$ μm; $E_F = 0.20$ eV, $\theta = 0$ °.

As shown in Figure 5, the width, upper and lower thresholds of the nonlinear OB hysteresis curve vary with different incident angles. It is obvious that the width of the hysteresis curve of the OB increases as the angle of incidence increases. Specifically, where $\theta = 0°$, the hysteresis curve width is $\Delta Y \approx 0.048 \times 10^6$ V/m, with an upper threshold of $|E_i|_{up} \approx 1.039 \times 10^6$ V/m, and a lower threshold of $|E_i|_{down} \approx 0.991 \times 10^6$ V/m; where $\theta = 3°$, the hysteresis curve width is $\Delta Y \approx 0.075 \times 10^6$ V/m, with an upper threshold of $|E_i|_{up} \approx 1.091 \times 10^6$ V/m, and a lower threshold of $|E_i|_{down} \approx 1.016 \times 10^6$ V/m. Overall, the hysteresis curve width increases by nearly 1.037×10^6 V/m. The above results show that the threshold of OB can be effectively reduced by reasonably adjusting the incidence angle, while achieving the control of the hysteresis curve width, providing another feasible method for the fabrication and design of optically bistable devices.

In addition, as illustrated in Figure 6, the transmittance and transmitted electric field will decrease obviously with the increase in the period of the photonic crystal, which is due to the fact that the increased thickness of the structure will reduce the transmitted light and increase the reflected light. The transmittance is about 0.55 when T = 3, but with the increase in the layer number, the transmittance will decrease to about 0.15 when T = 6.

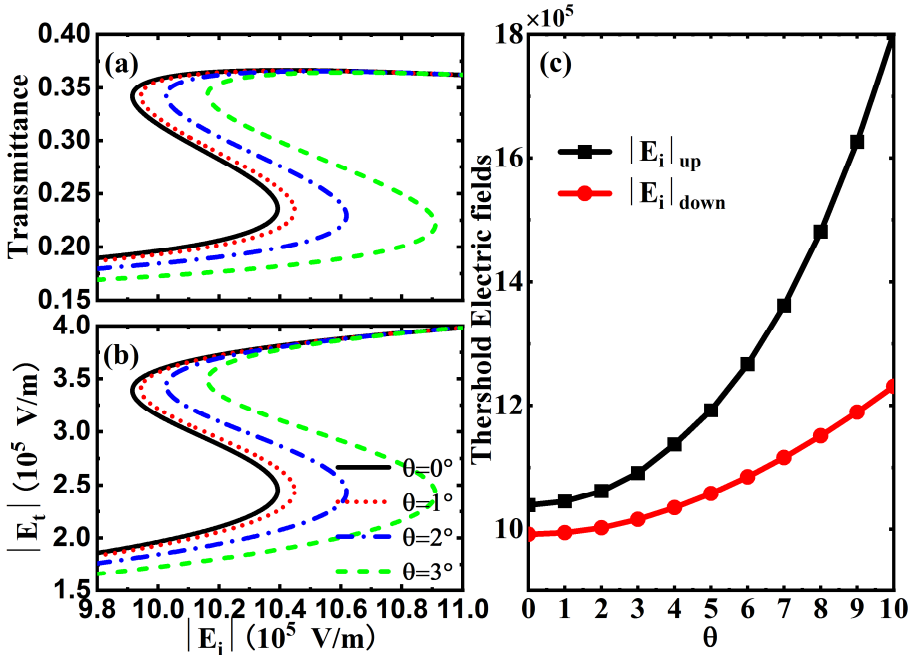


Figure 5. Dependence of (**a**) the transmittance and (**b**) the transmitted electric fields on the incidence electric field for different incident angles, where Λ = 300 μm, E_F= 0.20 eV, and τ= 0.9 ps. (**c**) Dependence of $|E_i|_{up}$ and $|E_i|_{down}$ on different incident angles.

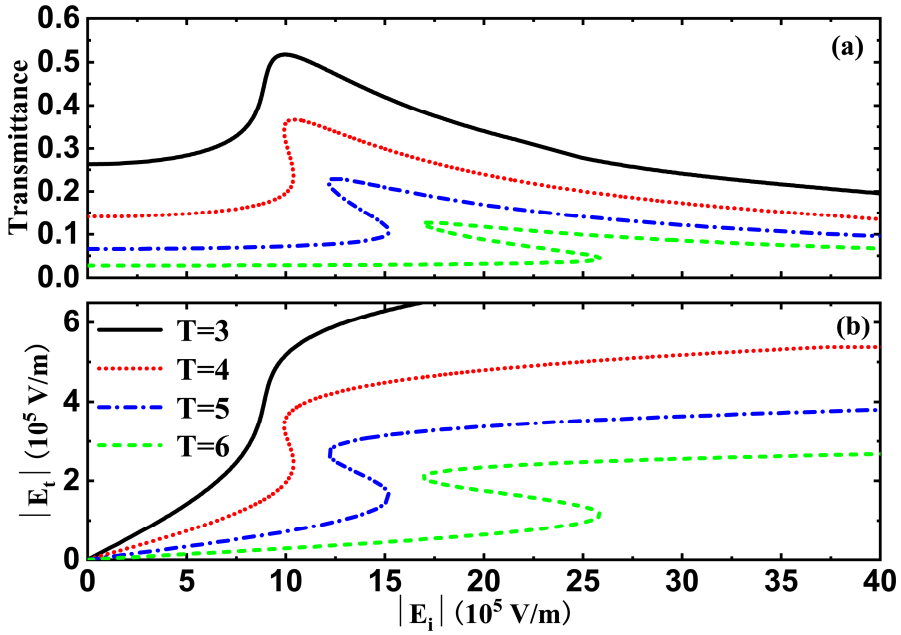


Figure 6. Dependence of (**a**) the transmittance and (**b**) the transmitted electric fields on the incidence electric field for period of photonic crystals, where Λ = 300 μm, E_F= 0.20 eV, and τ= 0.9 ps; θ= 0 °.

Finally, we also calculate the hysteresis curve relationship for the reflective OB as shown in Figure 7, where the relevant parameters involved remain the same as when calculating the transmitted OB. Figure 7a,b shows the reflectance and reflected electric field versus the incident electric field for the hysteresis curve at τ = 0.9 ps. When the Fermi energy level increases from 0.18 eV to 0.24 eV, the width of the hysteresis curve of OB increases and both the upper and lower thresholds increase, which is the same as the variation pattern of the transmitted OB shown in Figure 3.

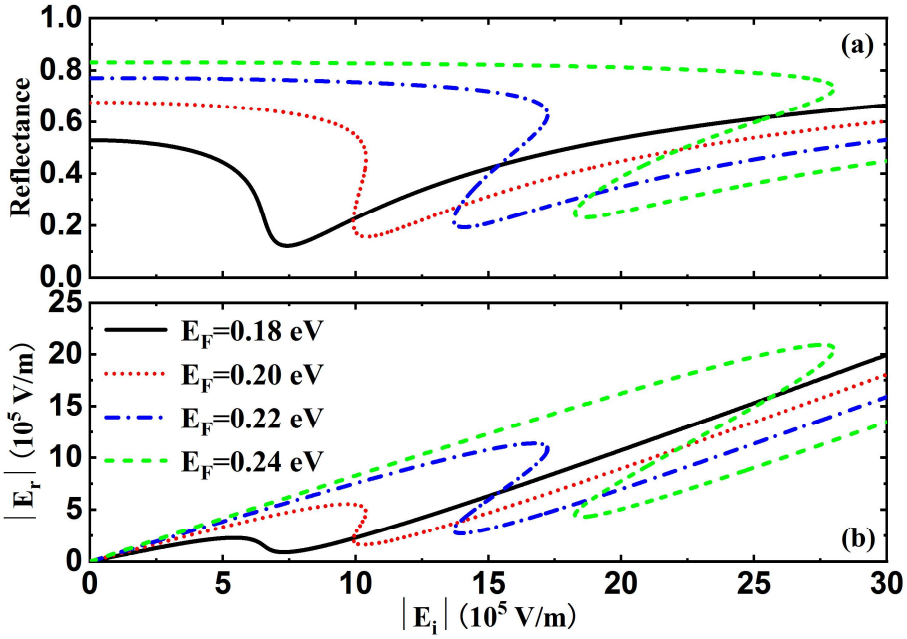


Figure 7. Dependence of (**a**) the reflectance and (**b**) the reflected electric fields on the incidence electric field for different 3D DSM Fermi energy, E_F, where τ= 0.9 ps; E_F= 0.20 eV.

4. Conclusions

In summary, we propose a multilayer hybrid structure consisting of two one-dimensional PhCs and a 3D DSM with which low-threshold tunable OB phenomena in the 1THz frequency range can be achieved. The results show that the local electric field enhancement caused by the PhC FP cavity has a positive effect on achieving a low threshold of OB. At the same time, the large nonlinear refractive index coefficient of the 3D DSM provides nonlinear conditions for the achievement of OB, and the threshold value of OB and the hysteresis curve width can be regulated by changing its relevant parameters. Through parameter optimization, optical bistability with a threshold approaching 10^5 V/m can be obtained, which reaches or is close to the range of the weak field. In addition, we calculated the multivalued functional relationships between the transmitted and reflected electric fields and the incident electric field using the transfer matrix method, knowing that the threshold of OB and the hysteresis curve width are regulated by the Fermi energy level and relaxation time of the 3D DSM. Our proposed low-threshold OB scheme has the characteristics of simple structure and easy preparation, and we believe that this low-threshold OB scheme is expected to find potential applications in related nonlinear optical devices.

Author Contributions: Conceptualization, formal analysis and writing—original draft, F.L., J.X. and Y.P.; writing—original draft preparation, F.L., J.L. and Y.P.; data curation and funding acquisition, Y.P. and M.H.; project administration and supervision, Y.P. and M.H.; data analysis and writing—review and editing, F.L., J.X., Y.P. and M.H. All authors have read and agreed to the published version of the manuscript.

Funding: This work was supported by the Natural Science Foundation of Hunan Province of China (grant no. 2020JJ4935), and Scientific Research Fund of Hunan Provincial Education Department (grant no. 21B0253).

Institutional Review Board Statement: Not applicable.

Informed Consent Statement: Not applicable.

Data Availability Statement: Not applicable.

Conflicts of Interest: The authors declare no conflict of interest.

References

1. Hu, X.; Jiang, P.; Ding, C.; Yang, H.; Gong, Q. Picosecond and low-power all-optical switching based on an organic photonic-bandgap microcavity. *Nat. Photonics* **2008**, *2*, 185–189. [CrossRef]
2. Yanik, M.F. All-optical transistor action with bistable switching in a photonic crystal cross-waveguide geometry. *Opt. Lett.* **2003**, *28*, 2506–2508. [CrossRef] [PubMed]
3. Shen, W.; Zhou, G.; Du, J.; Zhou, L.; Xu, K.; He, Z. High-speed silicon microring modulator at the 2 μm waveband with analysis and observation of optical bistability. *Photonics Res.* **2022**, *10*, A35–A42. [CrossRef]
4. Li, Y.N.; Chen, Y.Y.; Wan, R.G.; Yan, H.W. Dynamical switching and memory via incoherent pump assisted optical bistability. *Phys. Lett. A* **2019**, *383*, 2248–2254. [CrossRef]
5. Zhang, W.L.; Jiang, Y.; Zhu, Y.Y.; Wang, F.; Rao, Y.J. All-optical bistable logic control based on coupled Tamm plasmons. *Opt. Lett.* **2013**, *38*, 4092–4095. [CrossRef] [PubMed]
6. Masaya, N.; Akihiko, S.; Satoshi, M.; Goh, K.; Eiichi, K.; Takasumi, T. Optical bistable switching action of Si high-Q photonic-crystal nanocavities. *Opt. Express* **2005**, *13*, 2678–2687.
7. Maksimov, D.N.; Bogdanov, A.A.; Bulgakov, E.N. Optical bistability with bound states in the continuum in dielectric gratings. *Phys. Rev. A* **2020**, *102*, 033511. [CrossRef]
8. Chen, P.Y.; Farhat, M.; Alu, A. Bistable and self-tunable negative-index metamaterial at optical frequencies. *Phys. Rev. Lett.* **2011**, *106*, 105503. [CrossRef]
9. Xing, P.; Ma, D.; Kimerling, L.C.; Agarwal, A.M.; Tan, D.T.H. High efficiency four wave mixing and optical bistability in amorphous silicon carbide ring resonators. *APL Photonics* **2020**, *5*, 076110. [CrossRef]
10. Sakoda, K. *Optical Properties of Photonic Crystals*; Springer: Berlin, Germany, 2005.
11. Zhang, Y.; Zhao, Y.; Lv, R. A review for optical sensors based on photonic crystal cavities. *Sensor Actuat. A Phys.* **2015**, *233*, 374–389. [CrossRef]
12. Chen, X.; Chardin, C.; Makles, K.; Car, C.; Chua, S.; Braive, R.; Robert-Philip, I.; Briant, T.; Cohadon, P.F.; Heidmann, A. High-finesse Fabry-Perot cavities with bidimensional Si_3N_4 photonic-crystal slabs. *Light-Sci. Appl.* **2017**, *6*, 16190. [CrossRef] [PubMed]
13. Liu, J.T.; Liu, N.H.; Li, J.; Li, X.J.; Huang, J.H. Enhanced absorption of graphene with one-dimensional photonic crystal. *Appl. Phys. Lett.* **2012**, *101*, 666. [CrossRef]
14. Qi, D.; Wang, X.; Cheng, Y.; Chen, F.; Liu, L.; Gong, R. Quasi-periodic photonic crystal Fabry-Perot optical filter based on Si/SiO_2 for visible-laser spectral selectivity. *J. Phys. D Appl. Phys.* **2018**, *51*, 225103. [CrossRef]
15. Yacomotti, A.M.; Monnier, P.; Raineri, F.; Ben Bakir, B.; Seassal, C.; Raj, R.; Levenson, J.A. Fast thermo-optical excitability in a two-dimensional photonic crystal. *Phys. Rev. Lett.* **2006**, *97*, 143904. [CrossRef] [PubMed]
16. Parandin, F.; Bagheri, N. Design of a 2× 1 multiplexer with a ring resonator based on 2D photonic crystals. *Results Opt.* **2023**, *11*, 100375. [CrossRef]
17. Seraj, Z.; Soroosh, M.; Alaei-Sheini, N. Ultra-compact ultra-fast 1-bit comparator based on a two-dimensional nonlinear photonic crystal structure. *Appl. Opt.* **2020**, *59*, 811–816. [CrossRef]
18. Yacomotti, A.M.; Raineri, F.; Vecchi, G.; Monnier, P.; Raj, R.; Levenson, A.; Ben Bakir, B.; Seassal, C.; Letartre, X.; Viktorovitch, P.; et al. All-optical bistable band-edge Bloch modes in a two-dimensional photonic crystal. *Appl. Phys. Lett.* **2006**, *88*, 231107. [CrossRef]
19. Azadpour, F.; Bahari, A. All-optical bistability based on cavity resonances in nonlinear photonic crystal slab-reflector-based Fabry–Perot cavity. *Opt. Commun.* **2019**, *437*, 297–302. [CrossRef]
20. Donnelly, C.; Tan, D.T. Ultra-large nonlinear parameter in graphene-silicon waveguide structures. *Opt. Express* **2014**, *22*, 22820–22830. [CrossRef]
21. Falkovsky, L.A. Optical properties of graphene. *J. Phys. Conf. Ser.* **2008**, *129*, 012004. [CrossRef]
22. Gullans, M.; Chang, D.E.; Koppens, F.H.L.; de Abajo, F.G.; Lukin, M.D. Single-photon nonlinear optics with graphene plasmons. *Phys. Rev. Lett.* **2013**, *111*, 247401. [CrossRef] [PubMed]
23. Zhang, H.; Virally, S.; Bao, Q.; Ping, L.K.; Massar, S.; Godbout, N.; Kockaert, P. Z-scan measurement of the nonlinear refractive index of graphene. *Opt. Lett.* **2012**, *37*, 1856–1858. [CrossRef]
24. Jiang, T.; Kravtsov, V.; Tokman, M.; Belyanin, A.; Raschke, M.B. Ultrafast coherent nonlinear nanooptics and nanoimaging of graphene. *Nat. Nanotechnol.* **2019**, *14*, 838–843. [CrossRef] [PubMed]
25. Hendry, E.; Hale, P.J.; Moger, J.; Savchenko, A.K.; Mikhailov, S.A. Coherent nonlinear optical response of graphene. *Phys. Rev. Lett.* **2010**, *105*, 097401. [CrossRef]
26. Long, X.; Bao, Y.W.; Yuan, H.X.; Zhang, H.Y.; Dai, X.Y.; Li, Z.F.; Jiang, L.Y.; Xiang, Y.J. Low threshold optical bistability based on topological edge state in photonic crystal heterostructure with Dirac semimetal. *Opt. Express* **2022**, *30*, 20847–20858. [CrossRef]
27. Wan, X.; Turner, A.M.; Vishwanath, A.; Savrasov, S.Y. Topological semimetal and Fermi-arc surface states in the electronic structure of pyrochlore iridates. *Phy. Rev. B* **2011**, *83*, 205101. [CrossRef]
28. Orlita, M.; Basko, D.M.; Zholudev, M.S.; Teppe, F.; Knap, W.; Gavrilenko, V.I.; Mikhailov, N.N.; Dvoretskii, S.A.; Neugebauer, P.; Faugeras, C.; et al. Observation of three-dimensional massless Kane fermions in a zinc-blende crystal. *Nature* **2014**, *10*, 233–238. [CrossRef]

29. Young, S.M.; Zaheer, S.; Teo, J.C.; Kane, C.L.; Mele, E.J.; Rappe, A.M. Dirac semimetal in three dimensions. *Phys. Rev. Lett.* **2012**, *108*, 140405. [CrossRef]
30. Wang, Z.J.; Sun, Y.; Chen, X.Q.; Cesare, F.; Xu, G.; Weng, H.M.; Dai, X.; Fang, Z. Dirac semimetal and topological phase transitions in A_3 Bi (A = Na, K, Rb). *Phys. Rev. B* **2012**, *85*, 195320. [CrossRef]
31. Wang, Z.; Weng, H.; Wu, Q.; Dai, X.; Fang, Z. Three-dimensional Dirac semimetal and quantum transport in Cd_3As_2. *Phys. Rev. B* **2013**, *88*, 125427. [CrossRef]
32. Li, Q.; Kharzeev, D.E.; Zhang, C.; Huang, Y.; Pletikosić, I.; Fedorov, A.V.; Zhong, R.D.; Schneeloch, J.A.; Gu, G.D.; Valla, T. Chiral magnetic effect in $ZrTe_5$. *Nat. Phys.* **2016**, *12*, 550–554. [CrossRef]
33. Zhang, C.L.; Xu, S.Y.; Belopolski, I.; Yuan, Z.J.; Lin, Z.Q.; Tong, B.B.; Bian, G.; Alidoust, N.; Lee, C.C.; Huang, S.M.; et al. Signatures of the Adler–Bell–Jackiw chiral anomaly in a Weyl fermion semimetal. *Nat. Commun.* **2016**, *7*, 10735. [CrossRef] [PubMed]
34. Shekhar, C.; Nayak, A.K.; Sun, Y.; Schmidt, M.; Nicklas, M.; Leermakers, I.; Zeitler, U.; Skourski, Y.; Wosnitza, J.; Liu, Z.; et al. Extremely large magnetoresistance and ultrahigh mobility in the topological Weyl semimetal candidate NbP. *Nat. Phys.* **2015**, *11*, 645–649. [CrossRef]
35. Narayanan, A.; Watson, M.D.; Blake, S.F.; Bruyant, N.; Drigo, L.; Chen, Y.L.; Prabhakaran, D.; Yan, B.; Felser, C.; Kong, T.; et al. Linear magnetoresistance caused by mobility fluctuations in n-doped Cd_3As_2. *Phys. Rev. Lett.* **2015**, *114*, 117201. [CrossRef] [PubMed]
36. He, L.P.; Hong, X.C.; Dong, J.K.; Pan, J.; Zhang, Z.; Zhang, J.; Li, S.Y. Quantum transport evidence for the three-dimensional Dirac semimetal phase in Cd_3As_2. *Phys. Rev. Lett.* **2014**, *113*, 246402. [CrossRef]
37. Politano, A.; Chiarello, G.; Ghosh, B.; Sadhukhan, K.; Kuo, C.N.; Lue, C.S.; Vittorio, P.; Amit, A. 3D Dirac plasmons in the type-II Dirac semimetal $PtTe_2$. *Phys. Rev. Lett.* **2018**, *121*, 086804. [CrossRef]
38. Liu, Z.K.; Zhou, B.; Zhang, Y.; Wang, Z.J.; Weng, H.M.; Prabhakaran, D.; Mo, S.-K.; Shen, Z.X.; Fang, Z.; Dai, X.; et al. Discovery of a three-dimensional topological Dirac semimetal, Na_3Bi. *Science* **2014**, *343*, 864–867. [CrossRef]
39. Chen, R.Y.; Gu, G.D.; Zhang, S.J.; Schneeloch, J.A.; Zhang, C.; Li, Q.; Wang, N.L. Optical spectroscopy study of three dimensional Dirac semimetal $ZrTe_5$. *Phys. Rev. B* **2015**, *92*, 075107. [CrossRef]
40. Liang, T.; Gibson, Q.; Ali, M.N.; Liu, M.; Cava, R.J.; Ong, N.P. Ultrahigh mobility and giant magnetoresistance in the Dirac semimetal Cd_3As_2. *Nat. Mater.* **2015**, *14*, 280–284. [CrossRef]
41. Veldhorst, M.; Snelder, M.; Hoek, M.; Gang, T.; Guduru, V.K.; Wang, X.L.; Zeitler, U.; van der Wiel, W.G.; Golubov, A.A.; Hilgenkamp, H.; et al. Josephson supercurrent through a topological insulator surface state. *Nat. Mater.* **2012**, *11*, 417–421. [CrossRef]
42. Neupane, M.; Xu, S.-Y.; Sankar, R.; Alidoust, N.; Bian, G.; Liu, C.; Belopolski, I.; Chang, T.-R.; Jeng, H.-T.; Lin, H.; et al. Observation of a three-dimensional topological Dirac semimetal phase in high-mobility Cd_3As_2. *Nature* **2014**, *5*, 3786. [CrossRef] [PubMed]
43. Wang, T.L.; Cao, M.Y.; Zhang, Y.P.; Zhang, H.Y. Tunable polarization-nonsensitive electromagnetically induced transparency in Dirac semimetal metamaterial at terahertz frequencies. *Opt. Mater. Express* **2019**, *9*, 1562–1576. [CrossRef]
44. Ooi, K.J.; Ang, Y.S.; Zhai, Q.; Tan, D.T.; Ang, L.K.; Ong, C.K. Nonlinear plasmonics of three-dimensional Dirac semimetals. *APL Photonics* **2019**, *4*, 034402. [CrossRef]
45. Jiang, L.Y.; Guo, J.; Wu, L.M.; Dai, X.Y.; Xiang, Y.J. Manipulating the optical bistability at terahertz frequency in the Fabry-Perot cavity with graphene. *Opt. Express* **2015**, *23*, 31181–31191. [CrossRef] [PubMed]

Disclaimer/Publisher's Note: The statements, opinions and data contained in all publications are solely those of the individual author(s) and contributor(s) and not of MDPI and/or the editor(s). MDPI and/or the editor(s) disclaim responsibility for any injury to people or property resulting from any ideas, methods, instructions or products referred to in the content.